Regional distance shear-coupled *PL* propagation within the northern Altiplano, central Andes

Jennifer L. Swenson,* Susan L. Beck and George Zandt

Southern Arizona Seismic Observatory (SASO), Department of Geosciences, The University of Arizona, Tucson, AZ 85721, USA

SUMMARY

Properties of the shear-coupled *P* wavetrain (*SPL*) from regional earthquakes provide important information about the structure of the crust and upper mantle. We investigate broad-band seismic data from intermediate-depth earthquakes and develop a grid search technique using synthetic seismograms to study the sensitivity of *SPL* and to model the crustal structure of the northern Altiplano, central Andes.

Waveforms from an earthquake that occurred on 1994 December 12 within the Nazca slab beneath the Altiplano display a clear *SPL* wavetrain at the temporary stations deployed during the BANJO and SEDA experiments. We relocate this event and determine the moment tensor by inverting the complete long-period waveforms. With these source parameters fixed, we perform sensitivity analyses using a reflectivity technique to compute synthetic seismograms at a distance of 313 km (BANJO station 2, SALI). We find that, at this distance, the long-period *SPL* wavetrain is sensitive to the following model parameters, in order of decreasing sensitivity: crustal V_P/V_S, mantle V_P/V_S, average crustal velocity, crustal thickness, focal depth, distance (location), crustal Q_α and Q_β, and mantle velocity.

We develop a grid search method to investigate the four parameters of the crust/upper mantle model to which the synthetic seismograms are most sensitive at SALI (crustal V_P/V_S, mantle V_P/V_S, average crustal velocity, crustal thickness). Trade-offs exist among all four of the model parameters, resulting in a range of acceptable crustal models that provide excellent fits between the data and synthetic seismograms in the passband of 15–100 s at a single station. However, by using data at a *range* of distances (150–450 km) we find that the model that provides the best overall fit between the data and synthetic seismograms, and thus best approximates the average characteristics of the crust and upper mantle structure of the northern Altiplano, is characterized by an average crustal velocity of 6.0 km s^{-1}, a crustal Poisson's ratio (σ_{crust}) of 0.25 and a mantle Poisson's ratio (σ_{mantle}) of 0.27. The resulting models confirm previous estimates of low Poisson's ratios, low average crustal velocity and thick crust in the Altiplano.

Key words: body waves, crustal structure, seismic wave propagation, sensitivity, synthetic seismograms.

1 INTRODUCTION

1.1 Previous geophysical studies of the Altiplano

The Altiplano of the central Andes is a high plateau with an average elevation of 3.6 km which is part of an active continental mountain belt. The Altiplano is bounded to the

*Now at: Geophysics and Global Security Division, Lawrence Livermore National Laboratory, PO Box 808, L-206, Livermore, CA, USA. E-mail: swenson6@llnl.gov

west by an active volcanic arc (Western Cordillera) and to the east by fold and thrust belts (Eastern Cordillera and sub-Andean zone). Recent geophysical studies focusing on the crustal and upper mantle structure of the Altiplano indicate that the crust is thick with low average crustal *P*-wave velocities. An east–west seismic refraction profile at 21.2°S (Wigger *et al.* 1994) revealed that the Altiplano has thick crust and low average crustal *P*-wave velocities (5.9–6.1 km s^{-1}). The receiver function analyses performed by Beck *et al.* (1996) suggested that the central Altiplano crust is 60–65 km thick with a low crustal Poisson's ratio (0.25). These results are

consistent with the study of Zandt *et al.* (1996), who used waveform modelling to determine low average crustal *P*-wave velocities (6.0 km s^{-1}), a low crustal Poisson's ratio (0.25) and a crustal thickness of 65 km for the Altiplano. The results of Schuessler (1994) and Myers *et al.* (1998) also suggest low average *P*-wave velocities and a thick crust for the Altiplano of the central Andes. In this study we: (1) utilize broad-band waveforms recorded at regional distances to investigate the characteristics and sensitivity of the shear-coupled *P* wavetrain to certain parameters of the crust and mantle; (2) develop a single-station grid search technique in order to analyse efficiently a large number of combinations of crust and upper mantle properties; and (3) place constraints on the structure of the Altiplano.

1.2 Previous studies of shear-coupled *P* waves

Shear-coupled *P* waves are a long-period wavetrain resulting from the coupling of shear phases with *PL* waves in the crustal waveguide. As demonstrated by Oliver (1961) and Chander *et al.* (1968), the concept of an *SPL* wavetrain can be explained by a combination of ray theory and leaking-mode theory. Elastic strain energy radiated from the source as *SV* waves reaches the surface where it becomes partially trapped in the waveguide created by the crust. After it has become trapped, it travels the remaining distance from source to receiver as a leaking mode of the waveguide.

In the following discussions of the specific phases that constitute *SPL*, we make use of the nomenclature outlined in Båth & Stefánsson (1966): ray segments that are up-going in the crustal layer are represented by lowercase letters; ray segments that are down-going in the crustal layer are represented by uppercase letters; and the up-going rays (direct phases) from the mantle are represented by uppercase letters.

At regional distances, the *SPL* wavetrain contains *SsPn* (subsequently abbreviated as *sPn*), *SsPmp*, and multiples of *SsPmp* (e.g. *SsPmpPmp*). Several studies in recent years have noted the presence of and exploited the information contained in shear-coupled *P* waves (e.g. Singh *et al.* 1995; Langston 1996; Zandt *et al.* 1996; Zhu & Helmberger 1997). We build upon the results of Zandt *et al.* (1996), who documented the presence of the shear-coupled *P* wavetrain in regional seismograms from intermediate-depth earthquakes in the Nazca slab and modelled the waveforms to estimate an average crustal structure for the northern Altiplano.
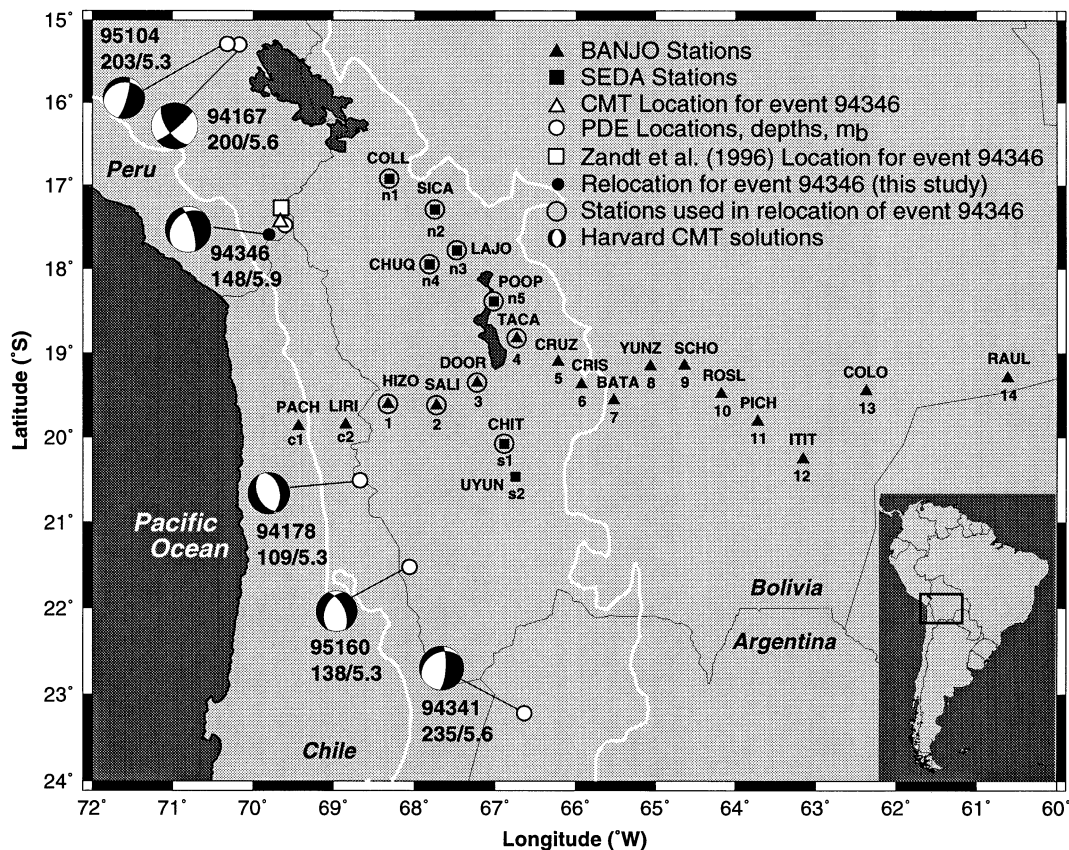

Figure 1. Map of west-central South America showing the locations of the BANJO (black triangles) and SEDA (black squares) portable broad-band seismic stations, PDE locations (white circles) and associated Harvard CMT solutions for selected intermediate-depth events that occurred during the BANJO and SEDA deployments. Also shown is the Harvard CMT location for event 94346 (white triangle), the location for event 94346 from Zandt *et al.* (1996), and the location for event 94346 determined in this study. Stations used in this study to determine the hypocentral location for event 94346 are circled. Numbers adjacent to event locations correspond to Julian day (YYDDD), depth/m_b. The 3500 m elevation line is contoured in white.

We explore the behaviour of shear-coupled *P* waves at regional distances by first conducting a series of sensitivity tests to identify the trade-offs among parameters such as crustal thickness, average crustal velocity, and crust and mantle Poisson's ratios. In order to utilize regional phases to determine velocity models, we must next understand the trade-offs among parameters at *single* stations. We therefore developed a single-station grid search technique to analyse efficiently a large number of combinations of crust and upper mantle properties, and investigate the structure of the northern Altiplano. We then expand our study to include multiple stations for more robust results.

2 DATA

Many of the earthquakes recorded at regional distances (100–1400 km) on the portable broad-band stations in the BANJO and SEDA arrays (see Beck *et al.* 1996) occurred at intermediate depths within the subducting Nazca slab; the epicentral locations of six of these are plotted in Fig. 1. Ray paths from earthquakes in the Nazca slab beneath the Altiplano travel from the slab, through the mantle and crust and directly to the BANJO and SEDA stations located on the margin of the plateau. These are relatively pure Altiplano ray paths, and, because these earthquakes were recorded at regional distances,
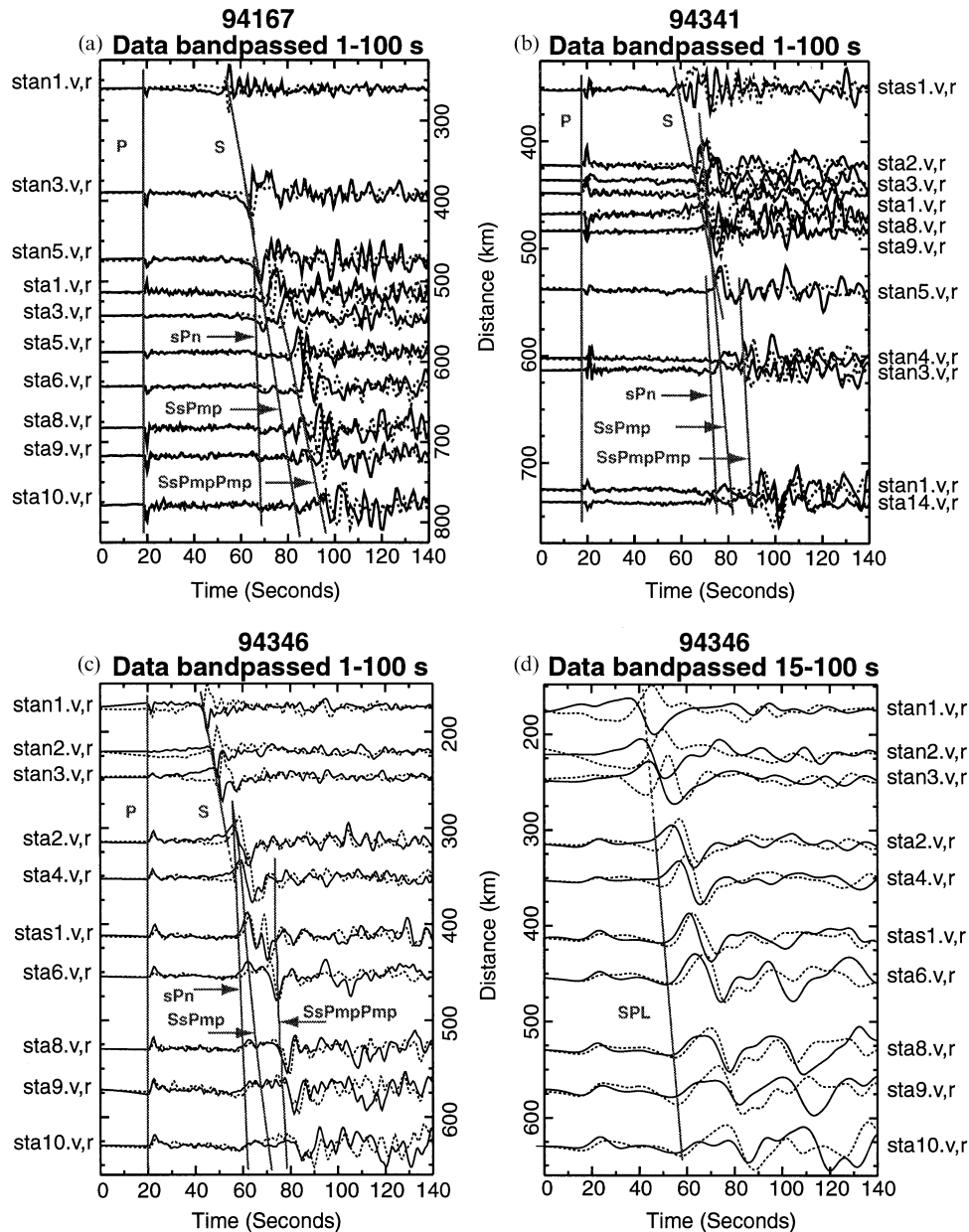

Figure 2. Example of data recorded by the BANJO and SEDA broad-band stations from events 94167 and 94341 (refer to Fig. 1). The instrument responses have been deconvolved from the data; traces are aligned on the *P* wave. (a) Vertical (solid line) and radial (dashed line) component data from event 94167, band-passed between 1 and 100 s. (b) Vertical (solid line) and radial (dashed line) component data from event 94341, band-passed between 1 and 100 s. (c) Vertical (solid line) and radial (dashed line) component data from event 94346, band-passed between 1 and 100 s. (d) Vertical (solid line) and radial (dashed line) component data from event 94346, band-passed between 15 and 100 s.

their waveforms are sensitive to details of the crust–mantle waveguide. Source-station geometries such as these will provide us with dense ray-path coverage for the central Andes.

The broad-band waveforms of intermediate-depth earthquakes recorded by BANJO and SEDA stations are rather complicated because, at regional distances, many phases arrive close together in time. At regional distances, the crust acts as a waveguide, and hundreds of reflections between the surface and Moho are important for waveform character (Lay & Wallace 1995). Figs 2(a) and (b) show the broad-band waveforms recorded on the BANJO and SEDA STS2 and Guralp sensors for the 1994 June 16 (m_b 5.6) and 1994 December 7 (m_b 5.6) events. In the following discussions, we will use the year and Julian day when referring to an earthquake; for example 1994 June 16 = 94167, and 1994 December 7 = 94341. Figs 2(c) and (d) show broad-band and band-passed data from an earthquake that occurred on 1994 December 12 (event 94346, m_b 5.9) (see also Fig. 1).

Note that all of the broad-band seismograms in Fig. 2 display a clear *P*-wave arrival, followed by a low-amplitude *SV* arrival, which was converted to *P* at the Moho (*Sp*), and then a complicated set of large-amplitude phases. These large-amplitude arrivals display *P*-wave apparent velocities. This wavetrain has prograde elliptical particle motion, which suggests that the energy left the earthquake source as *S* and converted to *PL* before reaching the recording stations. These independent analyses allowed us to identify the *SPL* wavetrain on the majority of seismograms recorded on the Altiplano. The dominant phase in the *SPL* wavetrain is *SsPmp* and its multiples (Fig. 2), which are created when the direct *SV* wave converts to a *P* wave at the free surface and becomes trapped in the crust because of post-critical *P*-wave reflection at the Moho (Langston 1996) (Fig. 3). Like all waves that have been supercritically reflected or transmitted at a discontinuity, *SsPmp* (and its multiples) undergoes a phase shift. The resulting waveform is a linear combination of the original waveform and its Hilbert Transform (Aki & Richards 1980). The shape and polarity of this post-critically reflected wave is controlled by the angle of incidence. The amplitude of *SsPmp* (and, at further distances, its multiples) is large because of the almost complete reflection at the Moho (Langston 1996).

Our study of shear-coupled *PL* propagation focuses on the data from event 94346 recorded at BANJO station SALI (station 2, distance 313 km). In the broad-band record at SALI (Fig. 3), we see a clear *P*-wave arrival, followed by low-amplitude *Ps* and *Sp* arrivals, and then the dominant *SsPmp* arrival. As we will demonstrate, the *Sp* arrival is an important phase in waveform modelling; *P*–*Sp* traveltimes provide important information regarding crustal thickness, average crustal velocities and mantle V_P/V_S ratios.

3 SOURCE AND SENSITIVITY STUDY

3.1 Determination of event hypocentre, and moment tensor inversion

An accurate hypocentral location is required for accurate fitting of regional seismograms. To constrain the event 94346 epicentre, *P*- and *S*-wave arrival times were picked from the vertical and radial component seismograms from the BANJO and SEDA stations on the Altiplano (Figs 1 and 2). We were careful to pick the *S* arrival using all three components so as
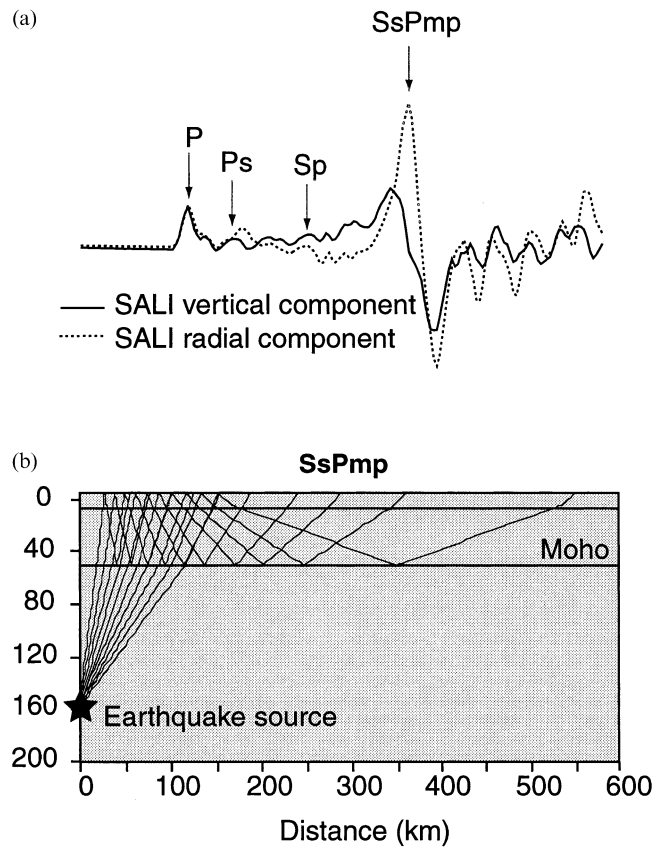

Figure 3. (a) Displacement traces for event 94346 (1994 December 12) from BANJO station 2 (SALI; distance = 313 km): vertical (solid line) and radial (dashed line) components, band-passed between 1 and 100 s. (b) Geometry of the *SsPmp* ray path.

not to confuse it with the *SsPmp* arrival. Using the epicentre and focal depth reported by the PDE catalogue as a starting point, we used the relocation program HYPO (Lienert 1994) to constrain the latitude, longitude, and origin time of event 94346. We used a simplified crustal/upper mantle model of the Altiplano in the relocation (65-km thick crust, $V_P = 6.0$ km s^{-1}, $\sigma_{crust} = 0.25$; from Zandt *et al.* 1996). The location that resulted in the lowest *P* and *S* residuals was 17.59°S, 69.80°W (Fig. 1).

To constrain the focal depth and to determine the source mechanism for this event, we performed a linear least-squares moment tensor inversion of the complete long-period waveforms, following the method of Randall *et al.* (1995). We used the same crustal model as described above and in Zandt *et al.* (1996).

We make use of the vertical, radial and transverse components of the time domain displacement seismograms from the BANJO stations on the Altiplano (1 to 4). The data are bandpass-filtered between 15 and 100 s because we want to reduce the sensitivity of the regional waveform to details of the crustal structure. A series of inversions is performed with different fixed depths between 125 and 210 km to provide a depth estimate for the earthquake. The quality of each data–synthetic seismogram fit is assessed visually and by an analysis of the least-squares error calculated by the inversion. A focal depth of 160 km resulted in the optimal data–synthetic fit; at this depth, the non-double-couple CLVD mechanism makes up 4.6 per cent of the total solution. The resultant focal

mechanism at a depth of 160 km (Fig. 4a) is similar to the Harvard CMT solution, and indicates normal faulting with a small component of strike-slip motion. The focal mechanism solution does not appear to be significantly sensitive to depth (Fig. 4a).

We perform an ellipticity analysis to confirm our depth estimate independently. We notice that, in the data, the largest peak in the *SPL* wavetrain on the vertical component leads the same peak on the radial component by approximately 3 s (Fig. 2d). This relationship in the long-period data is a result of the prograde elliptical particle motion of *SPL*. We use a reflectivity technique (described below) to compute synthetic seismograms for a range of focal depths. For each depth, we plot the particle motion of the large-amplitude *SPL* arrival in the synthetic seismograms (examples are shown in Fig. 4b). The depth at which the particle motion of the band-passed synthetic seismograms most closely approximates the particle motion of the data is 160 km, consistent with our depth estimate from the moment tensor inversion.

3.2 Waveform sensitivity

The sensitivity of the *SsPmp* arrival and the *SPL* wavetrain (interfering *SsPmp* arrivals) to parameters of the continental crust and mantle at a *given distance* must be understood before event 94346 can be used for modelling purposes. We have chosen a distance and azimuth of 313 km and 136°, respectively (SALI event-station geometry), for these sensitivity analyses. We computed approximately 500 synthetic seismograms, utilizing a reflectivity technique implemented by Randall (1994) to investigate the sensitivity of the complete waveforms to crustal thickness, focal depth, epicentral location (source–receiver

separation), average crustal velocity, crustal V_P/V_S ratio, Pn, mantle V_P/V_S ratio, and crustal Q_α and Q_β. Furthermore, we describe the trade-offs among the aforementioned parameters and use these analyses to characterize fully the behaviour of *SPL* propagation through the Altiplano.

Our standard starting model is the 8-layer approximation for the structure of the crust and upper mantle of the Altiplano that was used in the moment tensor inversion (65-km thick crust, $V_P = 6.0$ km s^{-1}, $\sigma_{crust} = 0.25$; from Zandt *et al.* 1996). We use the focal mechanism computed in the moment tensor inversion for the double-couple source in our model, placed at a depth of 160 km.

The resulting synthetic seismograms display the shear-coupled *P* waves we are investigating, and indicate the same prograde elliptical particle motion as is present in the data. Vertical and radial components of the broad-band (1–100 s) synthetic records and longer-period (15–100 s) synthetic records were analysed. The timing and amplitude of *P*, *Sp*, and *SsPmp* on the broad-band waveforms, and an analysis of *SPL* at longer periods, provide important information about properties of the crust and upper mantle structure. We make the following caveats with respect to the following analyses: the conclusions drawn in each subsection are restricted to the source–station geometry of SALI, and to the range of selected parameters.

In the following discussions of waveform sensitivity, we refer to the long-period shear-coupled *P* wavetrain (band-passed 15–100 s) as *SPL*, and refer to the individual components of the *SPL* wavetrain by their individual names (e.g. *SsPmp*, *sPn*, *Sp*).

We test eight parameters of the crust and upper mantle. Our sensitivity analyses suggest that the relative effects of these eight crust and upper mantle model parameters, in order of
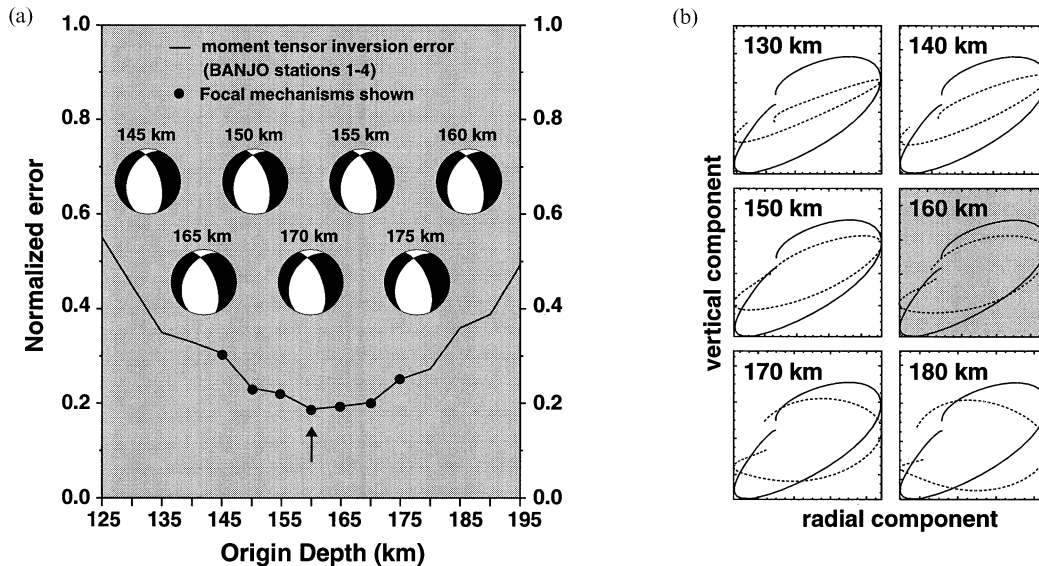

Figure 4. (a) Results from the moment tensor inversion for event 94346. The figure shows the depth versus normalized error curve for the range of focal depths tested. The arrow indicates the depth at which we obtained the best data–synthetic fit (160 km). The solid line represents the normalized error calculated by the inversion for the data–synthetic fit at these depths. Black dots indicate those depths for which focal mechanisms are shown. Note the relative insensitivity of the focal solution to depth. (b) Variation of particle motion with depth (130–180 km) in synthetic waveforms computed at a distance of 313 km. In each plot, the particle motion is shown for the large *SPL* arrival. Radial particle motion (*x*-axis) is plotted against vertical particle motion (*y*-axis). Particle motion for the data is shown with the solid line, and particle motion of the synthetic waveform is shown with the dashed line. Note the increase in ellipticity with increasing depth. As depth increases, particle motion becomes less rectilinear and more elliptical, and the amount of *P* energy relative to *SV* energy trapped in the crust–mantle waveguide approaches unity. The particle motion of *SPL* in the synthetic waveforms computed with a source depth of 160 km (shaded box) best fits the particle motion of *SPL* in the data.

decreasing effect on the computed synthetic waveform, are: crustal V_P/V_S, mantle V_P/V_S, average crustal velocity, crustal thickness, focal depth, distance (location), crustal Q_α and Q_β, and upper mantle Pn velocity. In the following paragraphs, we discuss in detail the four most influential model parameters, as well as trade-offs that exist among these four parameters. We highlight those model perturbations that result in noticeable changes in synthetic seismograms. Such relationships will be particularly valuable when attempting to fit synthetic seismograms to the data from SALI, for fine-tuning models, and also for future studies in this region incorporating additional event–station geometries.

3.2.1   *Sensitivity to crustal thickness*

We fixed the average crustal velocity at 6.0 km s^{-1} and computed synthetics for a source–receiver separation of 313 km for crustal thicknesses of 45, 55, 65 and 75 km to test the sensitivity of the waveforms to variations in crustal thickness. This range reflects the range of crustal thickness determined by previous geophysical studies (e.g. Beck *et al.* 1996). The broad-band and band-passed vertical component results of this sensitivity analysis are presented in Fig. 5(a) (note: in this and all subsequent waveform figures, seismograms have been aligned on the *P* wave peak). Because an increased crustal thickness causes the *S* wave to reach the Moho sooner, the most notable effect of the thickening of the crust is a decrease

in the time between the *P* and *Sp* arrivals. Hence, identifying the *Sp* arrival in the data can be very important and diagnostic of crustal thickness.

3.2.2   *Sensitivity to average crustal velocity*

We analyse the effect on the waveforms of varying the average crustal velocity by varying the *P*-wave velocity, maintaining average crustal *P*-wave velocities of 5.75–6.75 km s^{-1}. We maintain the V_P/V_S of our standard model (~ 1.73) by varying V_P (5.75–6.75 km s^{-1}) and then calculating the associated *S*-wave velocity in each model ($V_S = 3.32$–3.90 km s^{-1}). Selected results of this sensitivity analysis are presented in Fig. 5(b). The *P–Sp* relative traveltime decreases as the average velocity increases, suggesting that the change in the path of the *Sp* phase is more sensitive to the crustal velocity than the change in the path of the direct *P* wave. The *P* leg becomes shorter as crustal V_P increases because the *S*-to-*P* angle of refraction steepens. Increasing the average crustal velocity decreases the amplitude of the *SsPmp* arrival and decreases the *P–SsPmp* traveltime for the same reasons as given above for *Sp*.

Increasing the average crustal velocity decreases the amplitude of the large *SPL* peak more on the radial component than on the vertical component (band-passed records). This increase also decreases the *P–SPL* traveltime and decreases the relative traveltime between the peak and trough.

(a)
Variation in crustal thickness

(b)
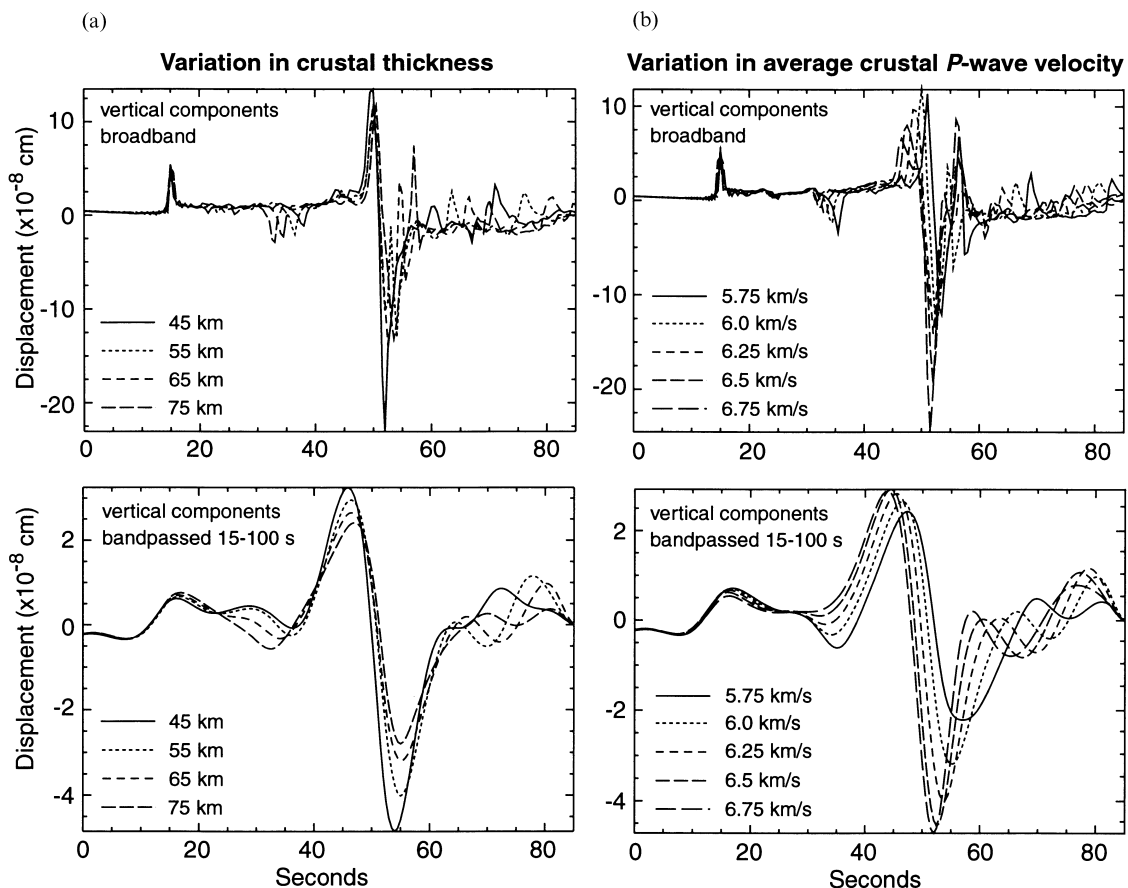**Variation in average crustal *P*-wave velocity**

Figure 5. (a) Synthetic seismograms computed to test sensitivity to variations in crustal thickness. Top: broad-band vertical components. Bottom: band-passed vertical components. (b) Synthetic seismograms computed to test sensitivity to variations in average crustal *P*-wave velocity. Top: broad-band vertical components. Bottom: band-passed vertical components.

3.2.3 Sensitivity to crustal V_P/V_S

We examine the sensitivity of the waveforms to V_P/V_S in the crust by fixing the P-wave velocity in each of the two crustal layers (5.5 km s^{-1} and 6.1 km s^{-1}, respectively) and allowing V_P/V_S to vary between 1.5 and 1.9 in each layer by changing the S-wave velocity. Increasing the V_P/V_S ratio increases the amplitude of the Sp arrival on the broad-band vertical component (Fig. 6a), but does not significantly affect the amplitude of the Sp arrival on the broad-band radial component. On the filtered records, increasing V_P/V_S has a greater effect on the amplitude of the large arrival on the radial component than on the vertical component. This is to be expected, since the radial components contain more S-wave energy. A low V_P/V_S (high V_S) in our model results in less contrast in V_S between the mantle and the crust, giving rise to lower amplitudes on our seismograms.

3.2.4 Sensitivity to mantle V_P/V_S

We analyse the sensitivity of the waveforms to the mantle V_P/V_S ratio by fixing Pn and allowing V_P/V_S to vary between 1.6 and 2.0 in each mantle layer. The starting crustal model was adjusted for this test by fixing Pn and calculating new Sn velocities for each V_P/V_S ratio. Selected results of this sensitivity analysis are presented in Fig. 6(b). In general, the magnitude and timing relations are similar to those observed in the crustal

V_P/V_S analyses (Fig. 6a). However, because the S wave travels further in the mantle than it does in the crust, varying V_S in the mantle results in longer traveltime differences than are seen in the crustal V_P/V_S sensitivity test. The analysis described in this section also suggests that the waveforms are more sensitive to Sn velocities (through a variation in V_P/V_S) than to Pn velocities (variation of Pn). A comparison of the synthetic seismograms computed to test sensitivity to crustal velocities and crustal V_P/V_S results in a similar conclusion.

3.2.5 Investigation of trade-offs among parameters

The trade-off between crustal thickness and average crustal velocity is commonly encountered in waveform modelling. The synthetic seismograms computed in this study for a range of crustal thicknesses and average crustal velocities also display this trade-off. This trade-off necessitates careful analysis of the long-period P–SPL and the broad-band P–$SsPmp$ traveltimes when investigating the effect of crustal thickness and average velocity variations on shear-coupled P waves in synthetic seismograms. We find that these waveforms are affected slightly more by changes to average crustal velocity than they are by changes to the crustal thickness (compare Figs 5b and a). We interpret this observation as a result of the complex interaction of phases (S, sPn and $SsPmp$) at this distance. We also note that the P–Sp traveltime is slightly more sensitive to crustal thickness than to average crustal velocity.
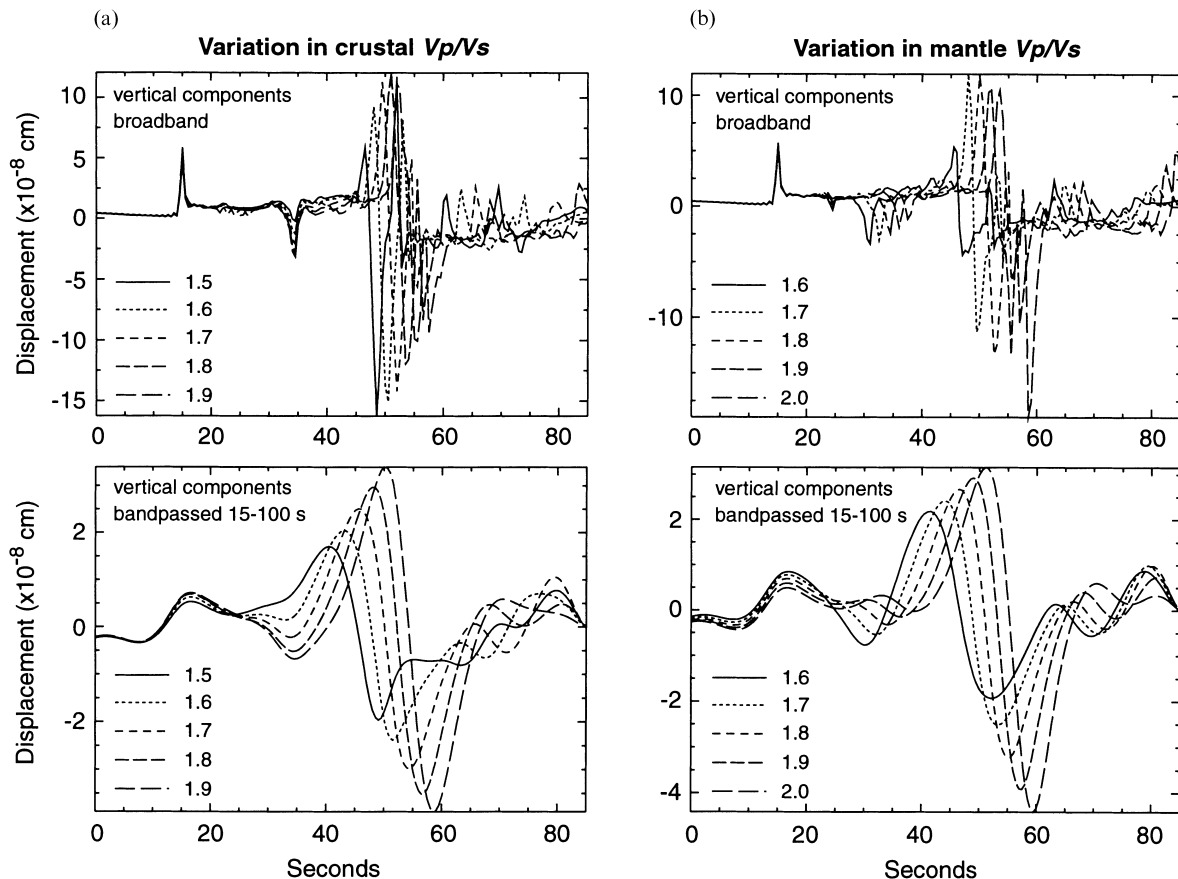

Figure 6. (a) Synthetic seismograms computed to test sensitivity to variations in crustal V_P/V_S. Top: broad-band vertical components. Bottom: band-passed vertical components. (b) Synthetic seismograms computed to test sensitivity to variations in mantle V_P/V_S. Top: broad-band vertical components. Bottom: band-passed vertical components.

It may also be difficult to isolate the effect of changing the crustal V_P/V_S ratio from that of changing the mantle V_P/V_S ratio (Figs 6a and b). The band-passed synthetic seismograms display this trade-off especially well. The behaviour of *Sp* on the broad-band synthetics is the key to isolating the differences between varying the crustal V_P/V_S and varying the mantle V_P/V_S. Increasing the mantle V_P/V_S ratio while keeping the crustal V_P/V_S ratio fixed increases the *P–Sp* traveltime and decreases the amplitude of the *Sp* arrival on the broad-band vertical and radial synthetic seismograms. Increasing the crustal V_P/V_S ratio while keeping the mantle V_P/V_S ratio fixed does *not* affect the *P–Sp* traveltime, and affects the amplitude of the *Sp* arrival only on the broad-band vertical component.

4   GRID SEARCH TO DETERMINE CRUSTAL STRUCTURE

We have used sensitivity analyses to characterize the behaviour of the regional *SPL* wavetrain and to isolate those four properties of the crust and upper mantle that most significantly affect regional *SPL* propagation. We next develop a comprehensive grid search method to test different combinations of the four most important model parameters. We use visual inspection and correlation coefficients to isolate the combination(s) of parameters that provides a best fit at SALI, and at the other BANJO and SEDA stations on the northern Altiplano, thereby constraining the crustal structure of the northern Altiplano.

Our starting model is based upon the simplest model that corresponds to previously obtained central Altiplano structure results (from Zandt *et al.* 1996): a 65-km thick crust with an average crustal *P*-wave velocity of 6.0 km s^{-1} and a crustal Poisson's ratio $\sigma_{crust} = 0.25$ ($V_P/V_S = 1.73$). Our grid search method investigates crustal thickness (55, 60, 65 and 70 km), average crustal *P*-wave velocity (6.0, 6.25 and 6.5 km s^{-1}; *S*-wave velocity calculated with a constant V_P/V_S ratio), crustal V_P/V_S (1.73, 1.78 and 1.84 or $\sigma_{crust} = 0.25$, 0.27 and 0.29), and mantle V_P/V_S (1.78, 1.84 and 1.91 or $\sigma_{mantle} = 0.27$, 0.29 and 0.31). For our grid search we use the source-station geometry at SALI (distance 313 km, azimuth 136°), the moment tensor computed in the moment tensor inversion (Section 3.1), and a source depth of 160 km
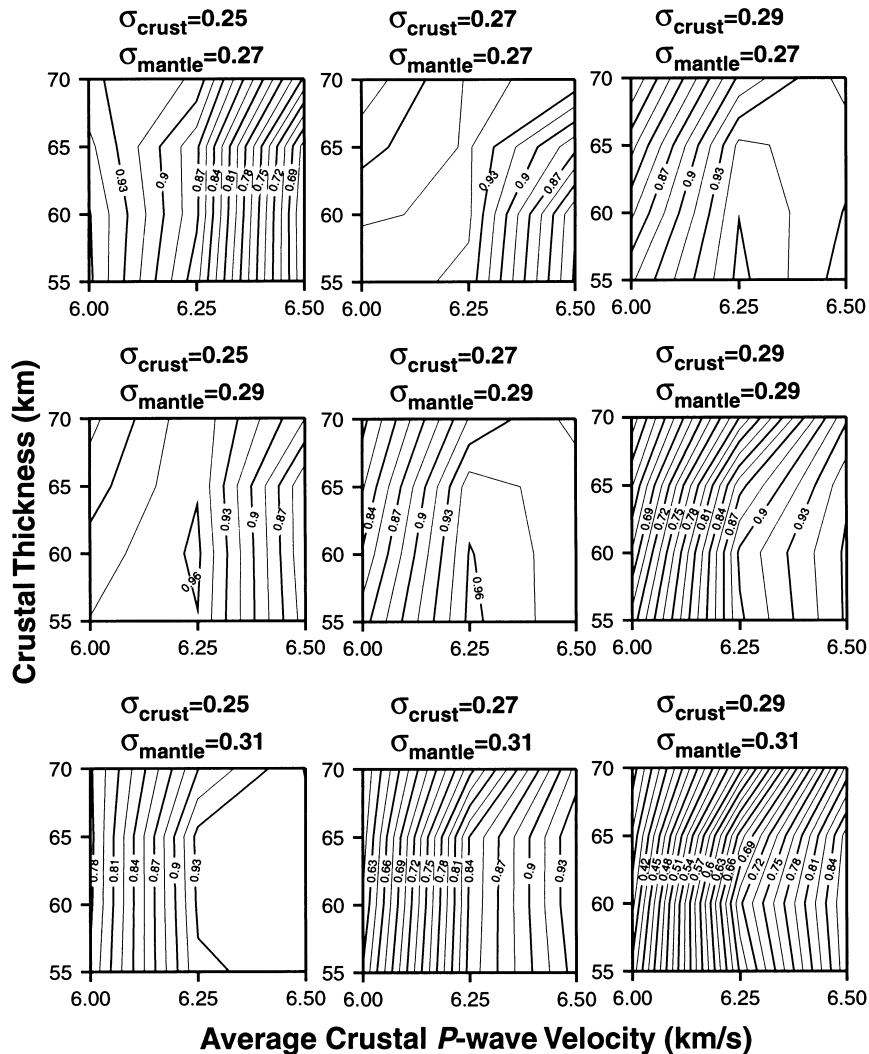

Figure 7. Results of the grid search using data recorded at SALI. Correlation coefficients are the averages of those calculated for the data and synthetic vertical and radial components. σ_{crust} increases from left to right; σ_{mantle} increases from top to bottom. A correlation coefficient of 1.0 indicates a perfect data–synthetic fit. Note the trade-offs between crustal thickness and velocity, as predicted by our sensitivity analyses.

This grid search results in the generation of 324 synthetic seismograms (vertical, radial and tangential components) from 108 unique combinations of grid search variables. The data and synthetic seismograms are band-passed between 15 and 100 s, cut to a length of 85 s and aligned on their pre-filtered *P*-wave peaks. We align the data and synthetic waveforms *a priori* to eliminate the possibility of our results being biased by a possible location error because the epicentres of the intermediate-depth earthquakes we analyse lie outside our network of stations.

Using the method outlined in Wallace *et al.* (1981), each vertical, radial and tangential component of the synthetic seismograms is numerically correlated with the corresponding component of the data from SALI. A correlation coefficient of 1.0 indicates a perfect fit between data and synthetic seismogram. We then average the correlation coefficients calculated for the vertical and radial components to give a single value for each model. The tangential component data and synthetic seismograms are very simple, and do not provide any constraints additional to those from the vertical and radial data; hence, the tangential data are not used in the grid search.

The averaged vertical and radial component numerical correlation results for all combinations of crustal thickness, average crustal *P*-wave velocity, σ_{crust} and σ_{mantle} are displayed in Fig. 7. The results clearly illustrate trade-offs that exist for these crustal and upper mantle parameters, as was predicted by our sensitivity analyses. For example, for a given set of σ_{crust}, σ_{mantle} and average crustal *P*-wave velocities, the data–synthetic fit decreases very slightly as the crustal thickness increases. As σ_{crust} increases, we obtain better fits with greater average crustal velocity. This correlation shifts to even larger average crustal velocities for higher σ_{mantle}. In general, correlation coefficients are lower for higher σ_{mantle}.

For the purposes of the following discussion, we divide our nine best models (correlation coefficients at SALI ≥ 0.95) into three classes of three models each, based on average crustal *P*-wave velocity. Class I models have an average crustal *P*-wave velocity of 6.0 km s^{-1}, crustal thicknesses of 55, 60 and 65 km, and $\sigma_{\text{crust}}/\sigma_{\text{mantle}} = 0.25/0.27$. Class II models have an average crustal *P*-wave velocity of 6.25 km s^{-1}, crustal thicknesses of 55 and 60 km, and $\sigma_{\text{crust}}/\sigma_{\text{mantle}} = 0.27/0.29$ and $0.29/0.27$. Class III models have an average crustal *P*-wave velocity of 6.5 km s^{-1}, crustal thicknesses of 55, 60 and 65 km, and $\sigma_{\text{crust}}/\sigma_{\text{mantle}} = 0.29/0.29$.

To illustrate the complexity in the trade-offs that exist among these four model parameters further, consider the trend of the correlation coefficients as average crustal velocity is increased.

(1) Within the Class I models ($V_P = 6.0$ km s^{-1}), we find it difficult to constrain the crustal thickness within the range of our search (Fig. 7). Crustal thicknesses of 55, 60 and 65 km provide very similar data–synthetic fits. Our difficulty in constraining the crustal thickness was predicted by the results of our sensitivity analysis, which suggested that, out of the four grid search parameters under consideration, perturbations to crustal thickness in the model result in the least amount of variability in *SPL*.

(2) If the average crustal *P*-wave velocity is increased to 6.25 km s^{-1}, a best fit is achieved using crustal thicknesses of 55 or 60 km and slightly higher σ_{crust} and σ_{mantle} (Class II models). We note that at this higher velocity, although the first half of the data and synthetic waveforms match better, we

sacrifice some of the good fit between the data and synthetics in terms of the amplitude of *SPL*.

(3) If the average velocity is increased to 6.5 km s^{-1} (Class III models), we match the initial portion of the waveforms much better, but we sacrifice the overall fit (timing and amplitude) of *SPL*. These examples illustrate the trade-offs in model parameters arising from the complexity of the *SPL* wavetrain at regional distances.

Synthetic seismograms computed for each Class I, II and III model discussed above provide excellent and similar fits to the data at SALI. Hence, at a single station with this source–station geometry we can determine a family of models that fit the long-period data. This can be very useful information, especially if additional constraints are available to eliminate some of the models. For example, as an independent check of the crustal and mantle V_P/V_S (or Poisson's ratios), we constructed a Wadati diagram using *P*- and *S*-wave picks at Altiplano stations for events similar in location to event 94346 (from Myers *et al.* 1998). The Wadati diagram suggests an average V_P/V_S ratio for the crust and mantle of 1.78, corresponding to an average Poisson's ratio of 0.27 (Fig. 8). Because direct *P*- and *S*-wave rays from events in the Nazca slab spend more time in the mantle than they do in the crust, we would expect that the average Poisson's ratio would be weighted towards the mantle value. Thus, the Poisson's ratio of 0.27 suggested by the Wadati diagram is a reasonable average for the crust and mantle in this region. Dorbath & Granet (1996) used *P*- and *S*-wave traveltimes picked from vertical component short-period records of local earthquakes to calculate an average V_P/V_S for the crust and mantle of the Altiplano of
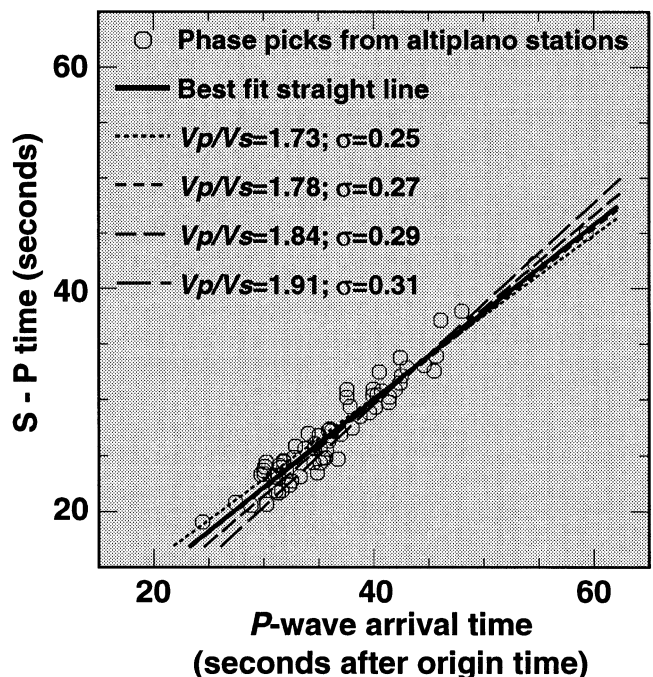

Figure 8. Wadati diagram constructed from *P*- and *S*-wave picks from Nazca slab earthquakes recorded by BANJO and SEDA stations located on the Altiplano. The solid black line is the slope of the best-fitting line through the phase picks. The slopes of the dashed lines represent several different V_P/V_S ratios. The best-fitting straight line corresponds to an average V_P/V_S ratio for the crust and mantle of 1.78, corresponding to an average Poisson's ratio of 0.27.

1.68, corresponding to a Poisson's ratio of approximately 0.23. Beck *et al.* (1996) determined a crustal Poisson's ratio of 0.25–0.26 for the Altiplano from receiver functions. Hence, there is no indication of a high crustal Poisson's ratio for the Altiplano. The models of our preferred set (Class I; see classification scheme above) have low average crustal velocities, crustal Poisson's ratios of 0.25, and mantle Poisson's ratios of 0.27.

Fig. 9(a) is a record section showing the fit between the vertical and radial component data and synthetics at the Altiplano stations for our preferred model, a member of the Class I category (average $V_P = 6.0$ km s^{-1}; crustal thickness 60 km; and $\sigma_{crust}/\sigma_{mantle} = 0.25/0.27$). For comparison, we show in Fig. 9(b) a record section showing the fit between the vertical and radial component data and synthetics at the Altiplano stations for one model in the Class III category (average $V_P = 6.5$ km s^{-1}; crustal thickness 60 km; and $\sigma_{crust}/\sigma_{mantle} = 0.29/0.29$). The data–synthetic waveform fit is clearly worse at distances of 150 km to 250 km for the model with the higher average V_P and higher σ_{crust} and σ_{mantle}.

Utilizing data from a range of distances when possible will help to eliminate models because trade-offs vary as a function of distance. We note that, in Figs 9(a) and (b), the quality of the data–synthetic waveform fit at Altiplano stations varies with distance, presumably reflecting the variations from a 1-D model. The crust of the Altiplano is represented as two simple layers; neither gradients or other subtle vertical variations are included. We conclude that, over all, the fit between the data and synthetic seismograms at some distances is better for the models with lower average crustal velocities ($V_P = 6.0$ km s^{-1}; Class I models) than for models with high average crustal velocities ($V_P = 6.5$ km s^{-1}; Class III models) and higher Poisson's ratios (compare Figs 9a and b).

We conclude that, of the 108 models tested in our grid search, the three models that provide the best fit between the data and synthetic seismograms at all of the Altiplano stations are characterized by low average crustal velocities, $\sigma_{crust} = 0.25$ and $\sigma_{mantle} = 0.27$ (Class I models).

The results of our sensitivity analyses suggest that crustal thickness will be most easily constrained in future studies by using the phase *Sp*; the timing and amplitude of this phase are particularly sensitive to changes in crustal structure. We infer from the results of Zandt *et al.* (1996) that the lack of a large-amplitude *Sp* arrival in our data is due to the presence of
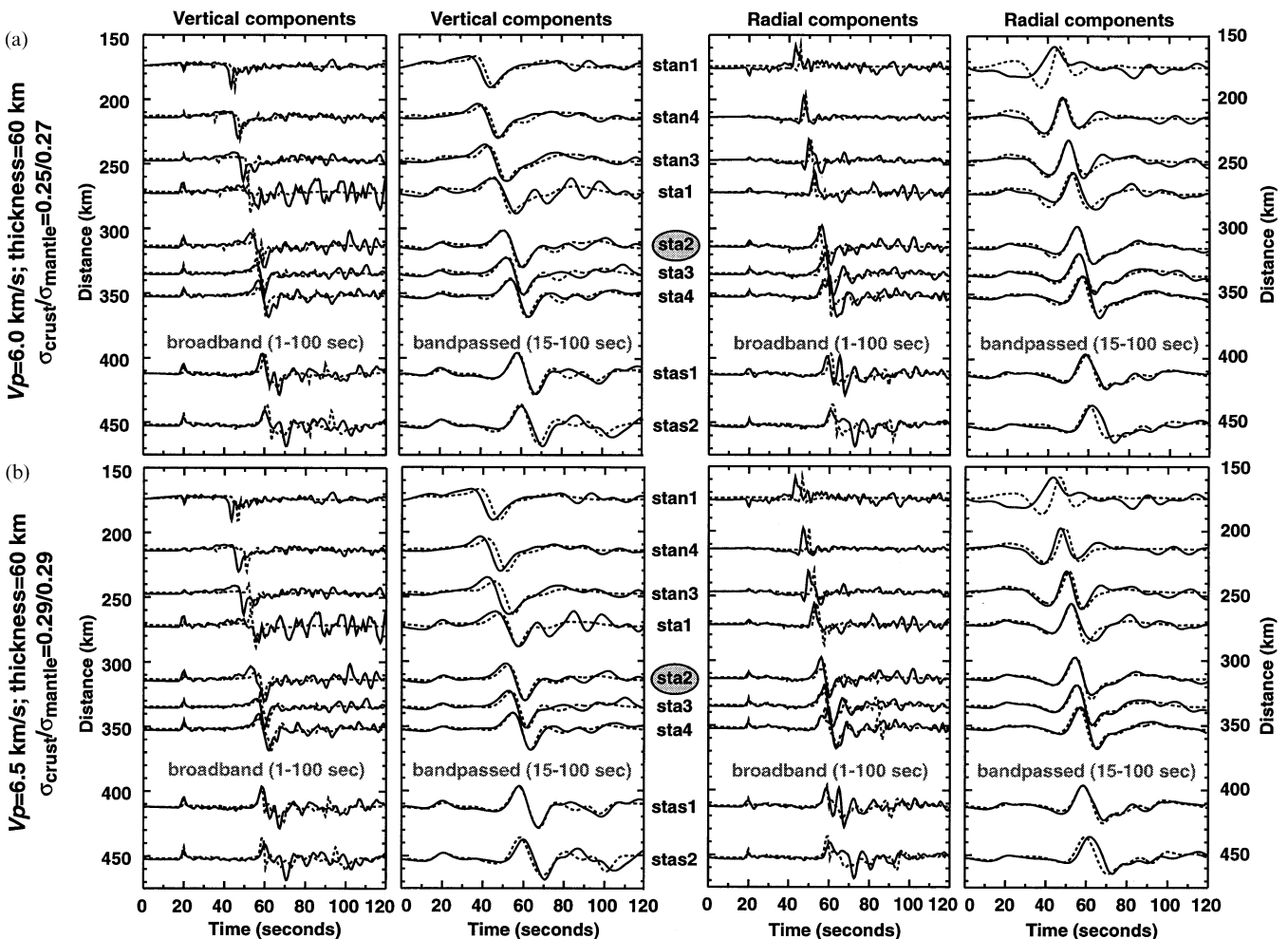

Figure 9. (a) Record sections showing the fit between the vertical and radial data (solid lines) and synthetic seismograms (dashed lines) at the Altiplano stations. Synthetic seismograms were computed using an average $V_P = 6.0$ km s^{-1}, crustal thickness of 60 km and $\sigma_{crust}/\sigma_{mantle} = 0.25/0.27$. (b) Record sections showing the fit between the vertical and radial data and synthetic seismograms computed using an average $V_P = 6.5$ km s^{-1}, crustal thickness of 60 km and $\sigma_{crust}/\sigma_{mantle} = 0.29/0.29$.

a velocity gradient at the Moho beneath the Altiplano. It is possible that different source–station geometries and/or a localized sharper Moho would result in a more well-defined *Sp* arrival; inclusion of these events in future structure analyses will allow us to constrain the crustal thickness better.

5 CONCLUSIONS

Broad-band regional waveform modelling is a useful technique with which to image the crust and upper mantle structure in the central Andes in Bolivia. Complicated arrivals near the *S*-wave arrival on regional broad-band data from event 94346 prompted us to use synthetic seismogram techniques to study the sensitivity of regional distance shear-coupled *P* waves to changes in the earth model and earthquake source parameters. After determining the depth, location and focal mechanism for this event, we perform sensitivity analyses using a reflectivity technique to compute synthetic seismograms. We find that the long-period *SPL* wavetrain is sensitive to the following model parameters, in order of decreasing sensitivity: crustal V_P/V_S (σ_{crust}), mantle V_P/V_S (σ_{mantle}), average crustal velocity, crustal thickness, focal depth, distance (location), crustal Q_α and Q_β, and upper mantle velocity (*Pn*).

We used a grid search method to investigate the four parameters of the crust/upper mantle model to which the synthetic seismograms are most sensitive at this distance (crustal thickness, average crustal *P*-wave velocity, σ_{crust}, σ_{mantle}). Reflectivity synthetic seismograms are computed in our grid search to determine a best crustal model for BANJO station SALI. Large trade-offs exist among all four of the model parameters, and there is a range of acceptable crustal models that provide excellent fits between the data and synthetic seismograms. The models that provide the best overall fit between the data and synthetic seismograms, and thus best approximate the average characteristics of the crust and upper mantle structure of the northern Altiplano, are characterized by an average crustal *P*-wave velocity of 6.0 km s^{-1}, $\sigma_{\text{crust}} = 0.25$ and $\sigma_{\text{mantle}} = 0.27$. With these parameters, crustal thicknesses of 55, 60 and 65 km provide very similar data–synthetic fits at SALI and at the other Altiplano stations. Future studies incorporating additional events with a variety of source–receiver geometries will allow us to constrain the crustal structure further.

REFERENCES

Aki, K. & Richards, P.G., 1980. *Quantitative Seismology, Volume One: Theory and Methods,* W.H. Freeman, San Francisco.

Båth, M. & Stefánsson, R., 1966. S–P conversion at the base of the crust, *Ann. Geofis.,* **19,** 119–130.

Beck, S.L., Zandt, G., Myers, S., Wallace, T.C., Silver, P. & Drake, L., 1996. Crustal thickness variations in the Central Andes, *Geology,* **24,** 407–410.

Chander, R., Alsop, L.E. & Oliver, J., 1968. On the synthesis of shear-coupled *PL* waves, *Bull. seism. Soc. Am.,* **58,** 1849–1877.

Dorbath, C. & Granet, M., 1996. Local earthquake tomography of the Altiplano and the Eastern Cordillera of northern Bolivia, *Tectonophysics,* **259,** 117–136.

Langston, C.A., 1996. The *SsPmp* phase in regional wave propagation, *Bull. seism. Soc. Am.,* **86,** 133–143.

Lay, T. & Wallace, T.C., 1995. *Modern Global Seismology,* Academic Press, Inc., San Diego.

Lienert, B.R., 1994. *Users Manual for HYPOCENTER 3.2: a Computer Program for Locating Earthquakes Locally, Regionally and Globally,* Hawaii Institute of Geophysics and Planetology, publ. 1-72.

Myers, S.C., Beck, S., Zandt, G. & Wallace, T., 1998. Lithospheric-scale structure across the Bolivian Andes from tomographic images of velocity and attenuation for *P* and *S* waves, *J. geophys. Res.,* **103,** 21 233–21 252.

Oliver, J., 1961. On the long period character of shear waves, *Bull. seism. Soc. Am.,* **51,** 1–12.

Randall, G.E., 1994. Efficient calculation of complete differential seismograms for laterally homogeneous earth models, *Geophys. J. Int.,* **118,** 245–254.

Randall, G.E., Ammon, C.J. & Owens, T.J., 1995. Moment tensor estimation using regional seismograms from a Tibetan plateau portable network deployment, *Geophys. Res. Lett.,* **22,** 1665–1668.

Schuessler, B.K., 1994. Crustal thickness variations in the Central Andes of South America determined from regional waveform modeling of earthquakes, *MSc thesis,* University of Arizona.

Singh, S.K., Santoyo, M.A. & Pacheco, J., 1995. Intermediate-depth earthquakes in Central Mexico; implications for plate waves, *Geophys. Res. Lett.,* **22,** 527–530.

Wallace, T.C., Helmberger, D.V. & Mellman, G.R., 1981. A technique for the inversion of regional data in source parameters studies, *J. geophys. Res.,* **86,** 1679–1685.

Wigger, P.J., Schmitz, M., Araneda, M., Asch, G., Baldzuhn, S., Giese, P., Heinsohn, W.-D., Martínez, E., Ricaldi, E.R., Röwer, P. & Viramonte, J., 1994. Variation in the crustal structure of the southern Central Andes deduced from seismic refraction investigations, in *Tectonics of the Southern Central Andes; Structure and Evolution of an Active Continental Margin,* pp. 23–48, eds Reutter, K.J., Scheuber, E. & Wigger, P.J., Springer, New York.

Zandt, G., Beck, S.L., Ruppert, S.R., Ammon, C.J., Rock, D., Minaya, E., Wallace, T.C. & Silver, P.G., 1996. Anomalous crust of the Bolivian Altiplano, Central Andes: constraints from broadband regional seismic waveforms, *Geophys. Res. Lett.,* **23,** 1159–1162.

Zhu, L. & Helmberger, D.V., 1997. Regional waveform calibration in the Pamir-Hindu Kush region, *J. geophys. Res.,* **102,** 22 799–22 813.